Supporting Information for

Oxygen Defects Engineering in Cobalt Iron Oxide Nanosheet for Promoted Overall Water Splitting

Chengying Guo [a]‡, Xuejing Liu [a]‡, Lingfeng Gao [a]‡, Xiaojing Ma [a], Mingzhu Zhao [a], Jinzhi Zhou [a], Xuan Kuang [a], Weiqiao Deng [b,c], Xu Sun [a] and Qin Wei [a]*

Table of contents

S1. Experiment and characterization

1. Experimental

1.1. Synthesis of $CoFe_2O_4$

To synthesize $CoFe_2O_4$, firstly 40 mL deionized water (DI) was added into a clean beaker. Then, 1.4 mmol urea (CH_4N_2O) and 0.01 mmol trisodium citrate (TSC) were added into DI to form a transparent and colorless solution. Finally, 0.4 mmol $FeCl_3 \cdot 6H_2O$ and 0.2 mmol $CoCl_2 \cdot 6H_2O$ were joined in the solution with the help of magnetic stirring to form a red solution. The received solution was stirred under magnetic stirring for 2 h. The acquired mixture was transferred and sealed in a 45 mL Teflon–lined autoclave then heated at 150 ^oC for 24 h. After reaction, the anti-spinel $CoFe_2O_4$ (CFO) was obtained successfully by centrifugation, washed with deionized water and ethanol, and then dried in vacuum 50 ^oC for about 6 h.

1.2. Synthesis of $CoFe_2O_4$ poor in oxygen vacancies

The catalyst of $CoFe_2O_4$ poor in oxygen vacancies (p-CFO) was obtained by annealing of the product that was synthesized in the previous step. The details of the experiment are 100 mg precursor annealed in N_2 atmosphere at 300 ^oC for 1 h.

1.3. Synthesis of $CoFe_2O_4$ rich in oxygen vacancies and grown on carbon cloth

$CoFe_2O_4$ rich in oxygen vacancies (r-CFO) was synthesized via the reduction reaction with $NaBH_4$ acting as the reductant. Firstly, 0.4 mol $NaBH_4$ was dissolved in 40 mL deionized water under the help of ultrasonication. Then, 50 mg p-CFO was dispersed in the as prepared $NaBH_4$ solution under ultrasonication for 3 h at room temperature. The black powder was then collected via centrifugation, which was also washed with water and ethanol for several times. Finally, the product was dried in vacuum for 5 hours. The fabrication of r-CFO @ CC are similar with the synthesis process for r-CFO except that the clean carbon cloth was added into the hydrothermal reaction system.

2. Electrochemical measurement

The electrochemical characterization was carried out on electrochemical station (CHI660B, China) using a classical three-electrode system in 1M KOH solution with O_2-saturated. As-produced sample was used for the working electrode, carbon rod as the auxiliary electrode, and Ag/AgCl electrode as the contrast electrode. The potential was calibrated against and converted to reversible hydrogen electrode (RHE). For working electrode, the glassy carbon (GC) electrode with the dimater of 3 mm was adopted as the electrode, after which the catalyst gel was droped onto it. For the preparation of catalyst gel, 5 mg of as-synthesized materials was dispersed in the 1 mL tailor-made solution of water/ethanol (7 : 3). Then, 50 μL of superpolymer (Nafion solution, 5 wt%) was added to obtain a homogeneous emulsion with the help of

sonication. 4 μL of the obtained solution was dropped on the clearly GC electrode. Specifically, the surface area of the glassy carbon was about 0.07 cm^2. The mass loading value was calculated to be 0.285 mg cm^{-2}, which is similar with the reported literature [1-3], confirming that the comparison between our as synthesized catalyst with the literature is believable. The preparation of Pt/C or RuO_2 decorated GC electrode is similar with the r-CFO coated GC electrode, except that the catalyst gel was prepared with Pt/C or RuO_2 being adopted as the catalyst. And, as for the r-CFO@CC electrode prepared by the in-situ growth, the carbon cloth (CC) with the size of (1.5*1*0.1) cm^3 was adopted as the catalyst suppoter (mass loading of about 1.51 mg cm^{-2}). The mass loading was obtained via the difference value between clean carbon cloth and carbon cloth with catalysts. Then the CC electrode was fixed via the electrode holder with GC colleator. Meanwhile, the mass loading of Pt/C and RuO_2 decorated CC is similar with r-CFO@CC. 20 times of CV was carried out with the scan rate of 100 mV s^{-1} to stabilize the catalyst in the voltage range of 1.02 ~ 1.82 V (vs. RHE). Next, polarization curve was proceed by linear sweep voltammetry at a sweep rate of 5 mV s^{-1} in O_2 pre-saturated 1.0 M KOH. At the same time, the polarization curves of all catalysts were calculated with iR compensation using the software of CHI660B. Furthermore, the measurement of Ac impedance was recorded at the frequency range of 0.1 mHz to 100 kHz, take-off potential of 1.55 V (vs. RHE) and the amplitude of 5 mV. To confirm the excellent stability, the around-the-clock of cyclic voltammetry with a scan rate of 100 mV s^{-1} was carried out for 1000 cycles between 1.02 V and 1.82 V (vs. RHE), after which LSV was performed at 5 mV s^{-1}. What's more, the turnover frequency (TOF) and the number of active sites were received from the methods previous reported. [4, 5]

3. Characterization

The internal morphologies feature of as obtained catalysts was examined with a Transmission electron microscope (H-800 microscope, Hitachi, Japan). The transmission electron microscopy images (TEM) of catalysts were collected on a JEOL-2100 transmission electron microscope using an acceleration voltage of 200 kV. The external morphologies as well as the distribution of elements of the catalysts were gathered by Helios FIB SEM at 10.0 kV. Powder XRD patterns for the crystalline phase analysis were recorded using Rigaku Smart Lab 9 kW. Spectral information was collected in the extent of 10° ~ 70° 2θ with a step width of 0.01°/2θ. X-ray photoelectron spectra (XPS) were elucidated by ESCALAB 250 electron energy spectrometer (Thermo Fisher Scientific, USA) and Monochromated Al Kα 150 W was used to the X-ray excitation source. Solid UV spectrum was recorded in a Shimadzu UV-3101PC spectrometer (Japan). All the electrochemical measurement was recorded on electrochemical station (CHI660B).

S2. XPS survey spectra of CFO, p-CFO and r-CFO

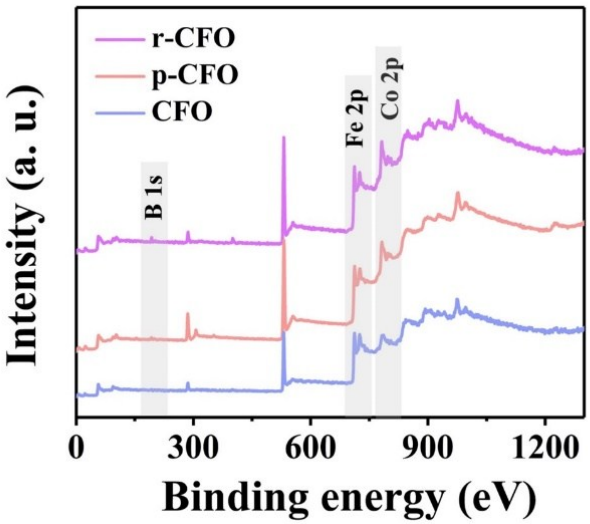

Figure S1. The XPS survey spectrum of CFO, p-CFO and r-CFO.

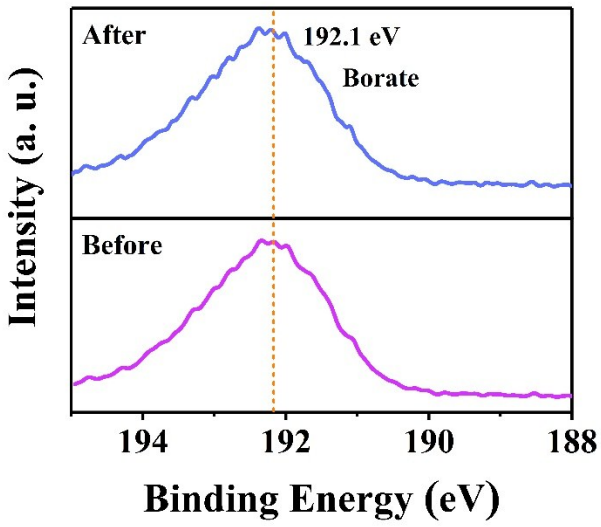

Figure S2. B1s spectrum of r-CFO before and after OER reaction.

S3. SEM of CFO and p-CFO

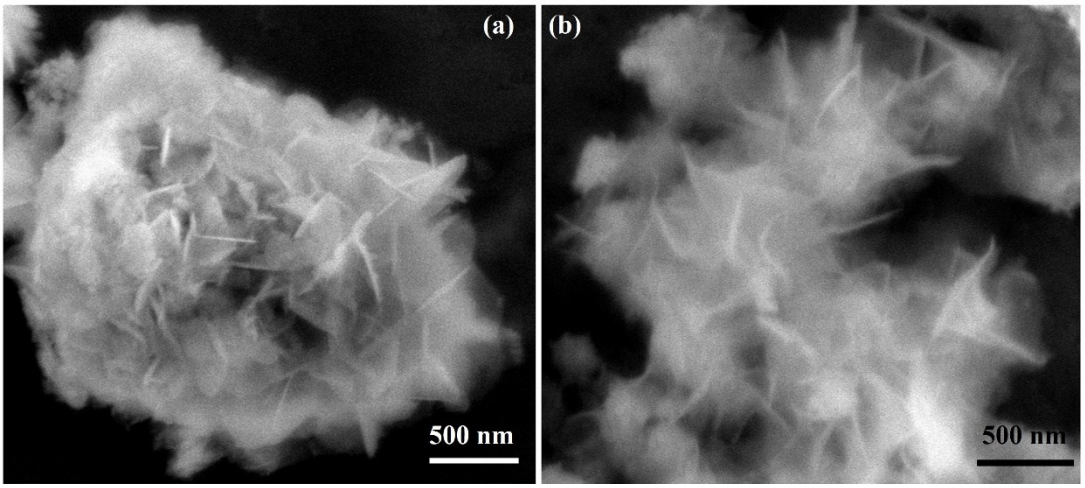

Figure S3. The SEM images of CFO and p-CFO. (a) SEM images of CFO. (b) SEM images of p-CFO.

S4. HRTEM of r-CFO

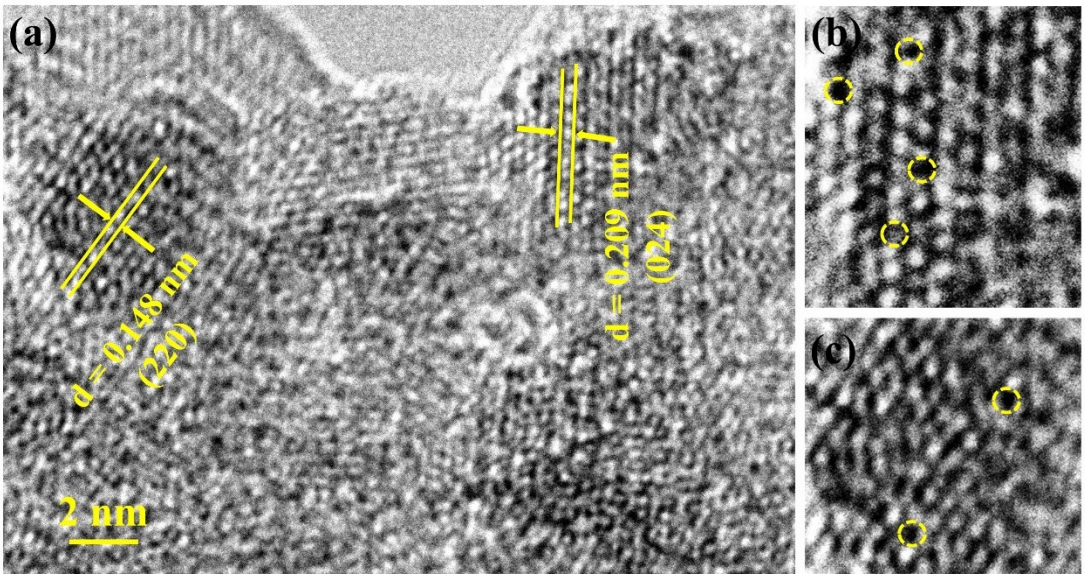

Figure S4. (a) HRTEM of r-CFO, (b) and (c) Magnified HRTEM images of r-CFO from which the vacancies region was deteced.

S5. EDS spectrum of r-CFO

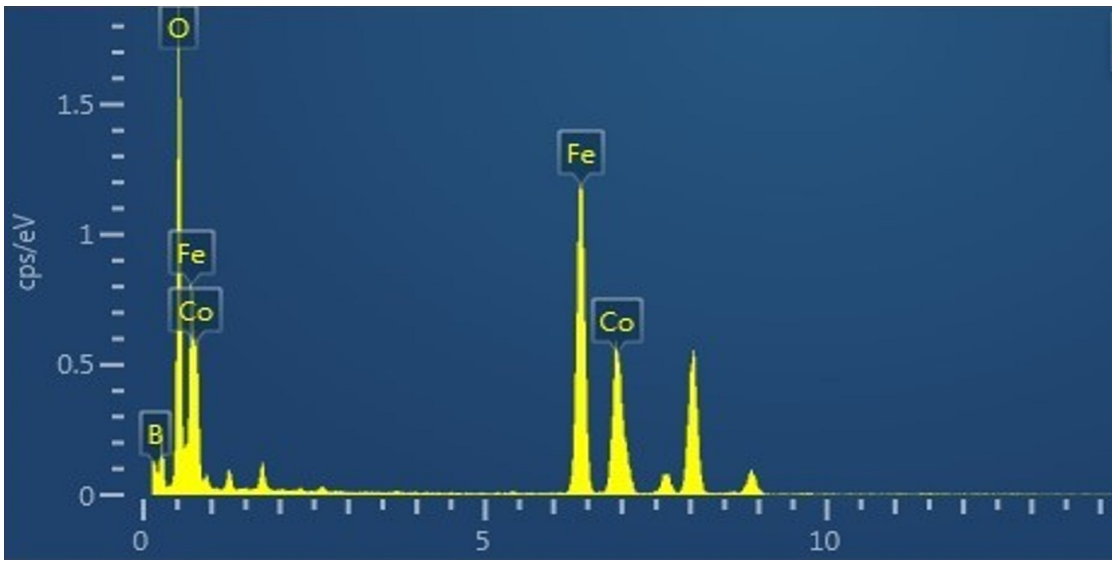

Figure S5. EDS spectrum of r-CFO.

S6. Equivalent circuit for modeling the impedance results

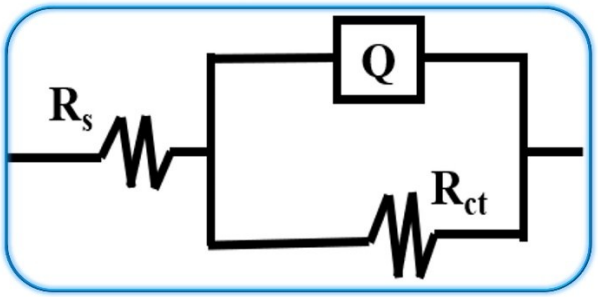

Figure S6. Equivalent circuit for modeling the impedance results.

S7. Cyclic voltammetry curves of CFO, p-CFO and r-CFO

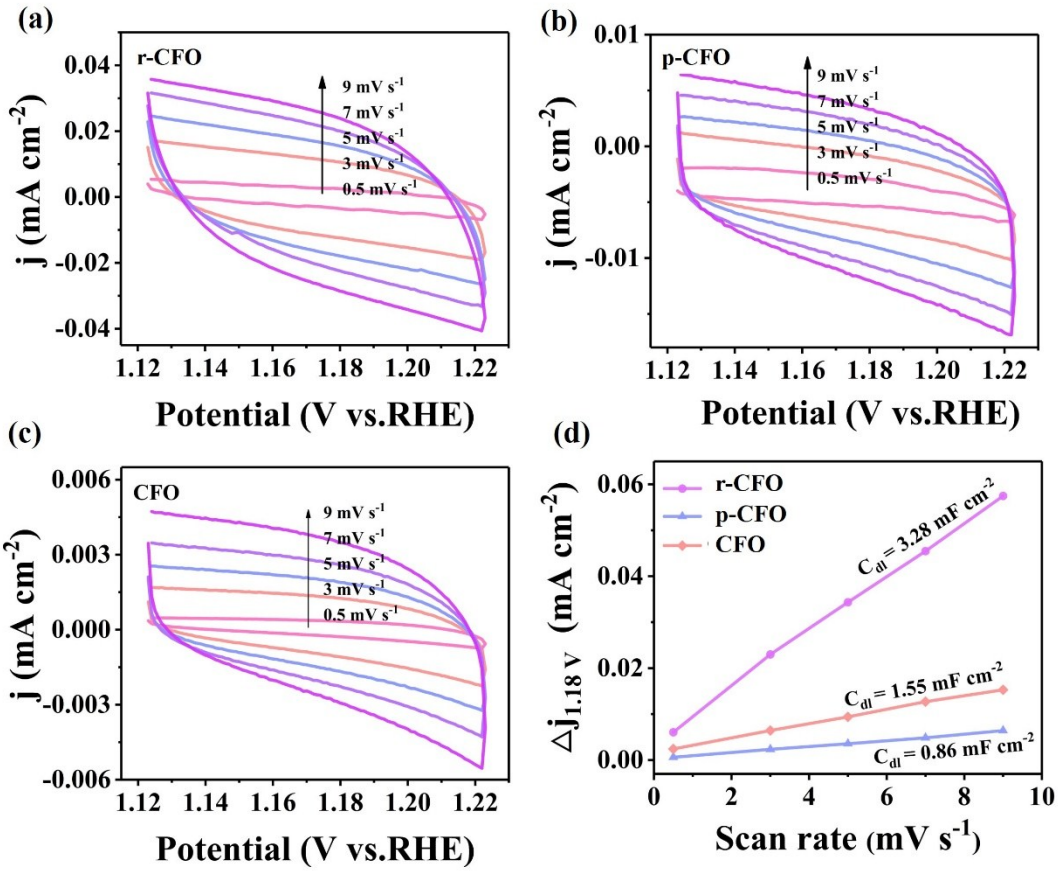

Figure S7. Characterization of electrochemical behavior of CFO, p-CFO and r-CFO. CVs of (a) r-CFO, (b) p-CFO and (c) CFO catalysts measured in 1.0 M KOH solution at scan rates from 0.5 to 9 mV s^{-1}. (d) Current density as a function of the scan rate for the different electrodes at 1.18 V vs. RHE, from which the C_{dl} was well calculated.

S8. Current density normalized by the C_{dl} of CFO, p-CFO and r-CFO

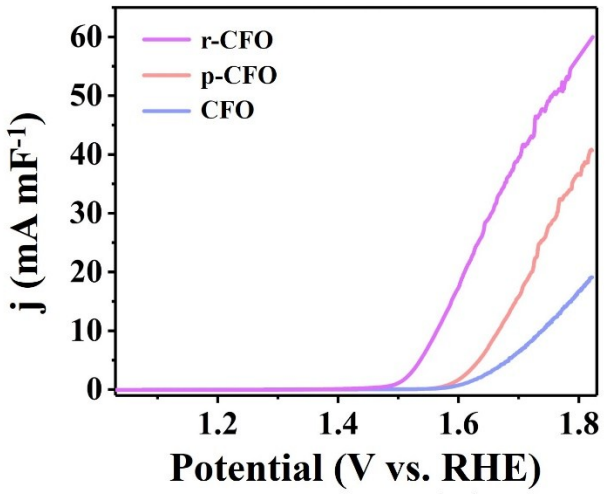

Figure S8. Polarization curves of CFO, p-CFO and r-CFO normalized by the C_{dl}.

S9. Stability measurement of r-CFO catalyst

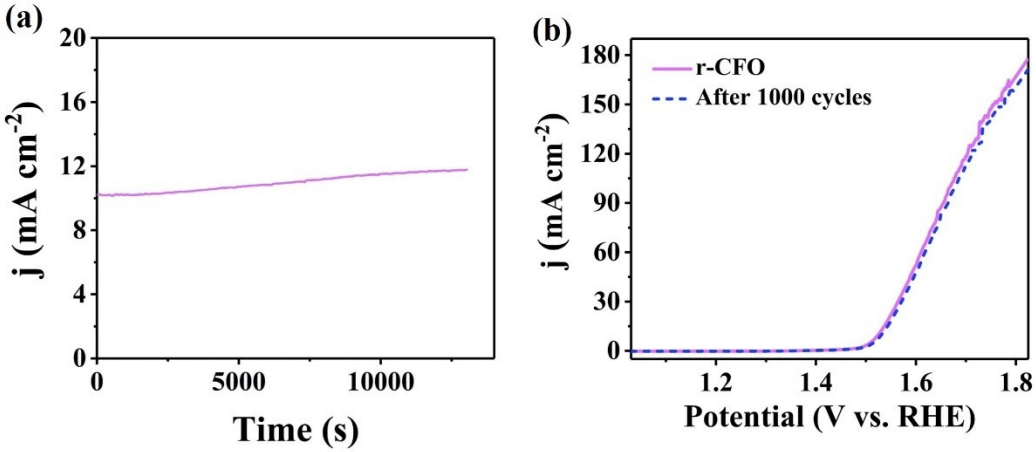

Figure S9. Stability measurement for OER. (a) Long time durability at overpotential of 280 mV. (b) I-V curves of r-CFO before and after 1000 cycles.

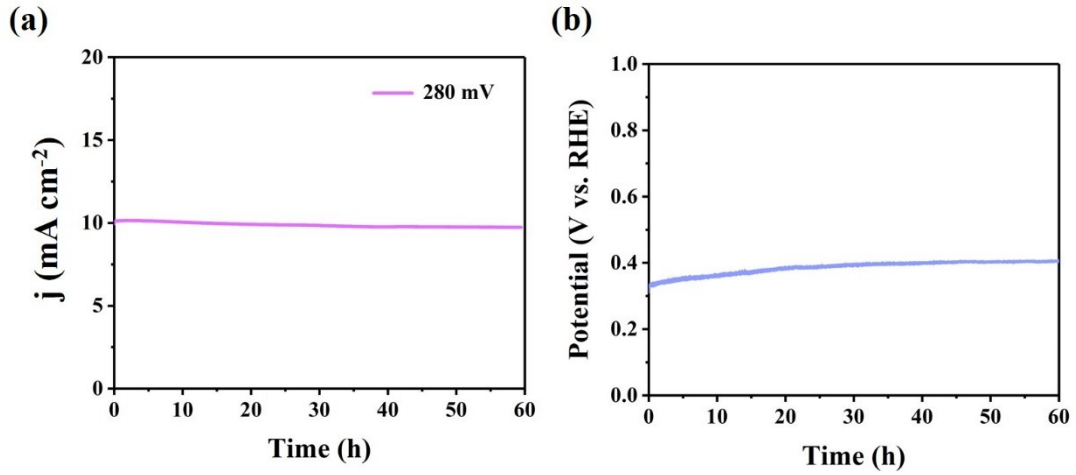

Figure S10. (a) The chronoamperometry curves of r-CFO for OER under overpotential of 280 mV for about 60 h. (b) The chronopotentiometry curve of r-CFO for OER, with the current being set at 30 mA cm^{-2}.

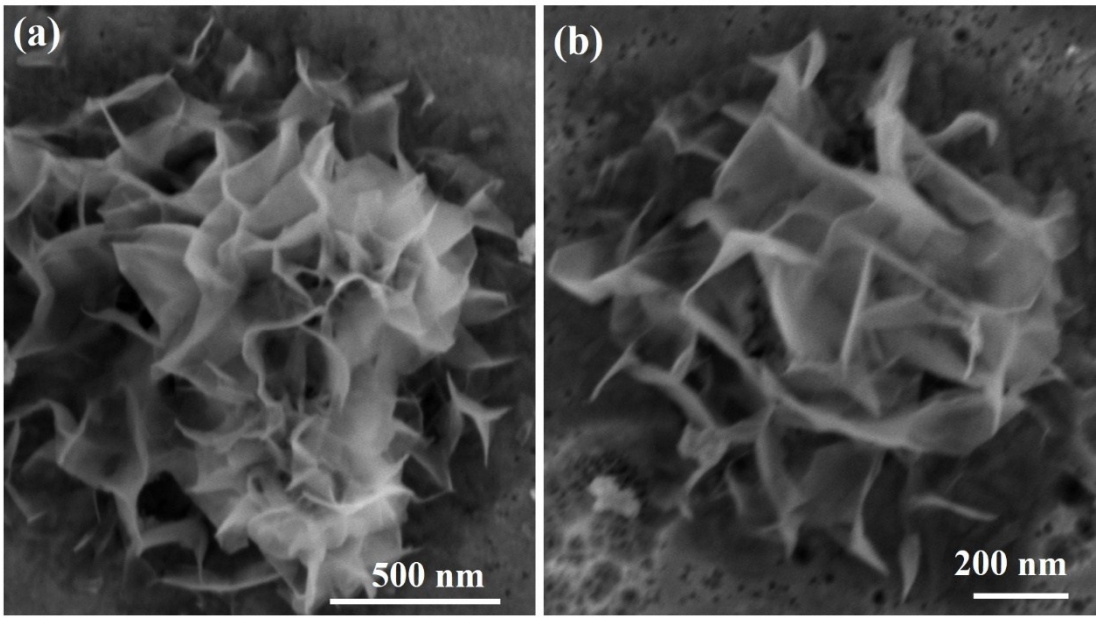

Figure S11. SEM images of r-CFO after the OER process (r-CFO-OER). The r-CFO-OERwas collected from the GC electrode after the OER reaction.

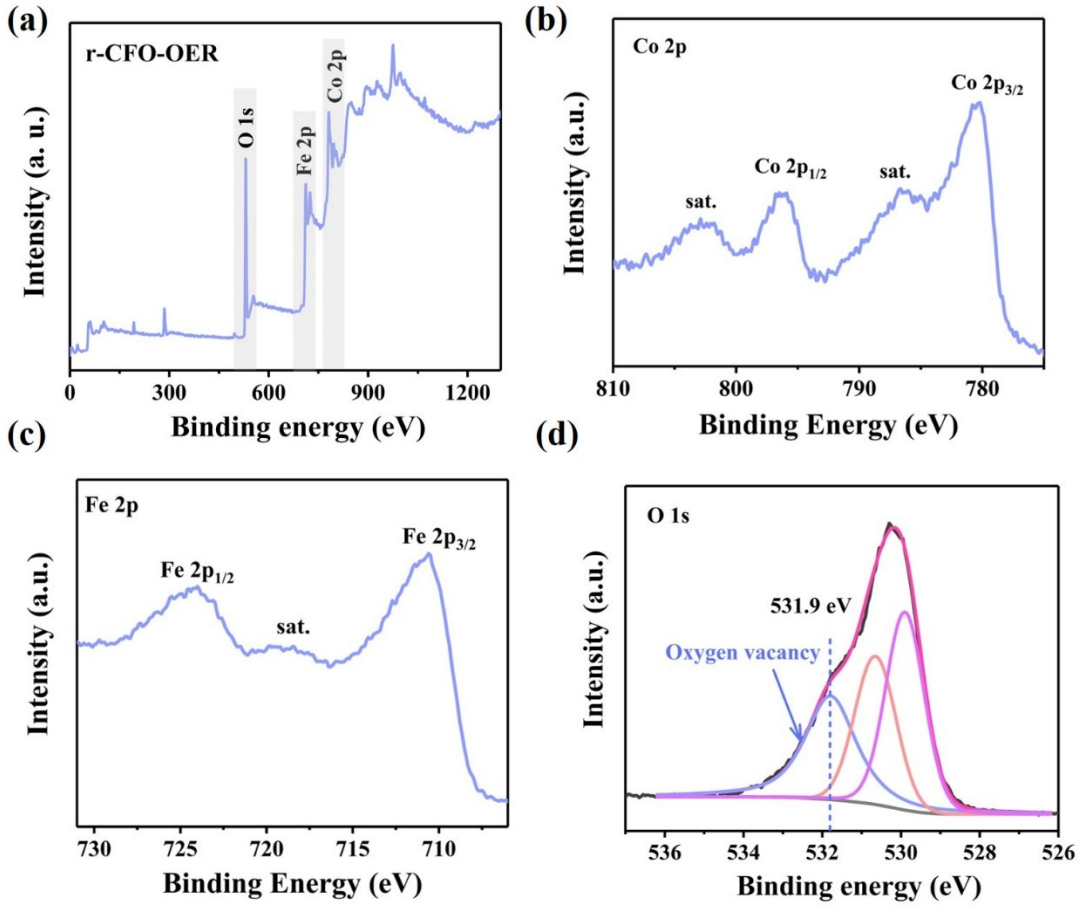

Figure S12. The XPS spectra of r-CFO-OER. (a) The survey spectrum of r-CFO-OER. (b), (c) and (d) The spectra for Co 2p, Fe 2p and O 1s of r-CFO-OER, respectively.

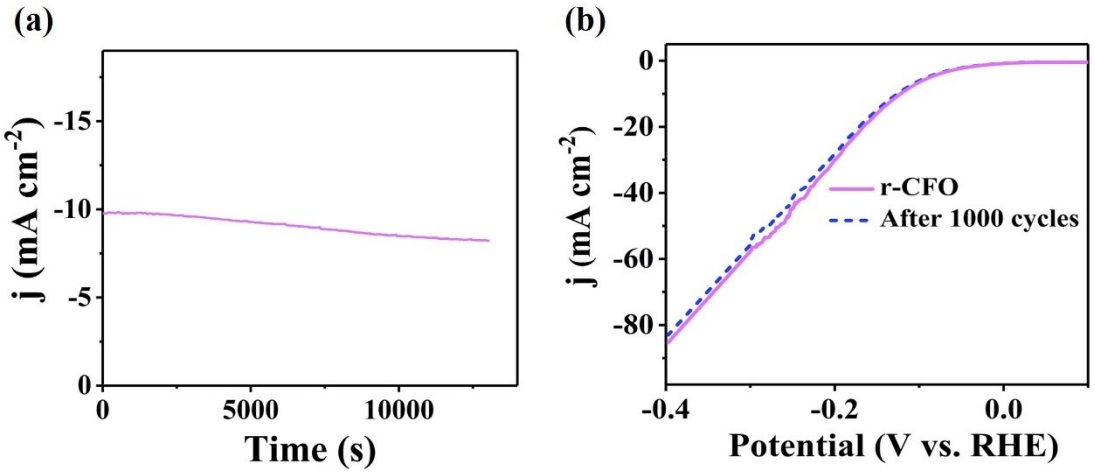

Figure S13. Stability measurement for HER. (a) Long time durability at overpotential of 121 mV. (b) I-V curves of r-CFO before and after 1000 cycles.

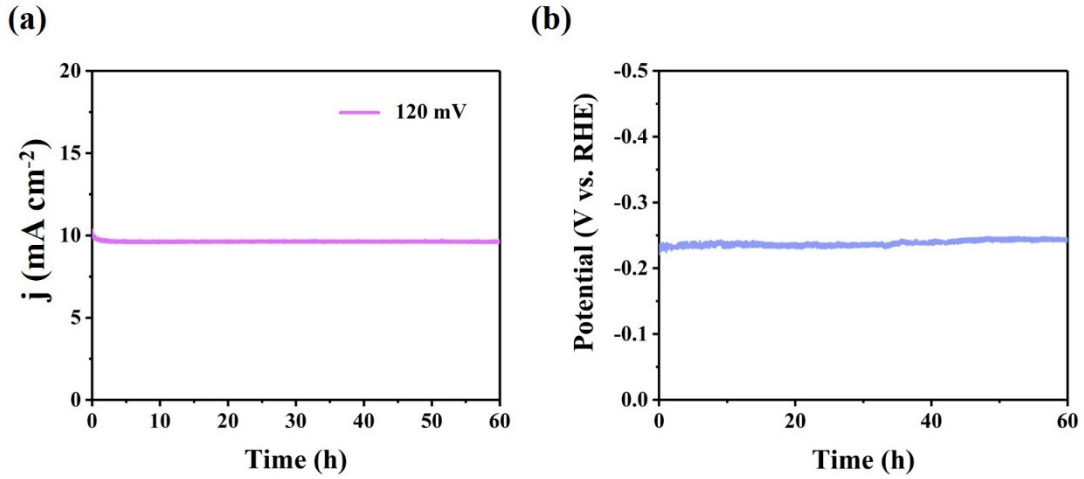

Figure S14. (a) The chronoamperometry curves of r-CFO for HER under overpotential of 120 mV for about 60 h. (b) The chronopotentiometry curves of r-CFO for HER, with the current being set at 30 mA cm^{-2}.

S10. SEM of r-CFO @ CC

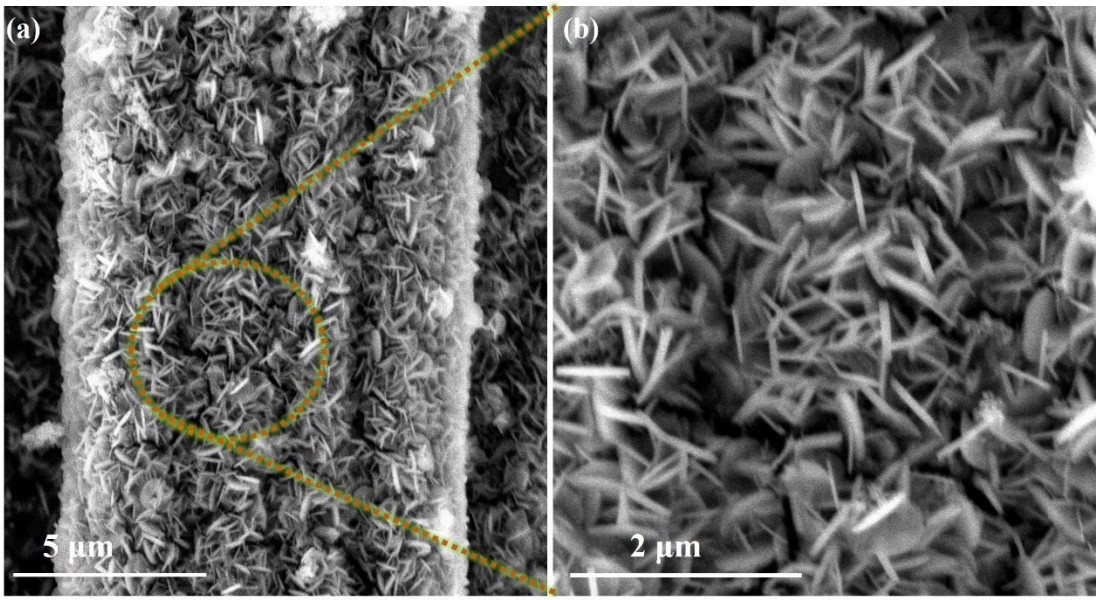

Figure S15. The SEM images of r-CFO grown on carbon cloth (r-CFO@CC). (a) SEM image of r-CFO grown on carbon cloth. (b) Amplificatory SEM image of r-CFO grown on carbon cloth.

S11. Stability test of r-CFO@CC

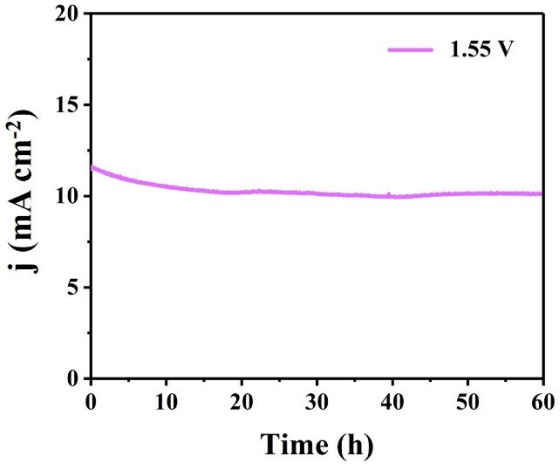

Figure S16. The chronoamperometry curves of r-CFO@CC for the long time water spitting test. The voltage was set to be 1.55 V.

S12. SEM of r-CFO @ CC after water splitting

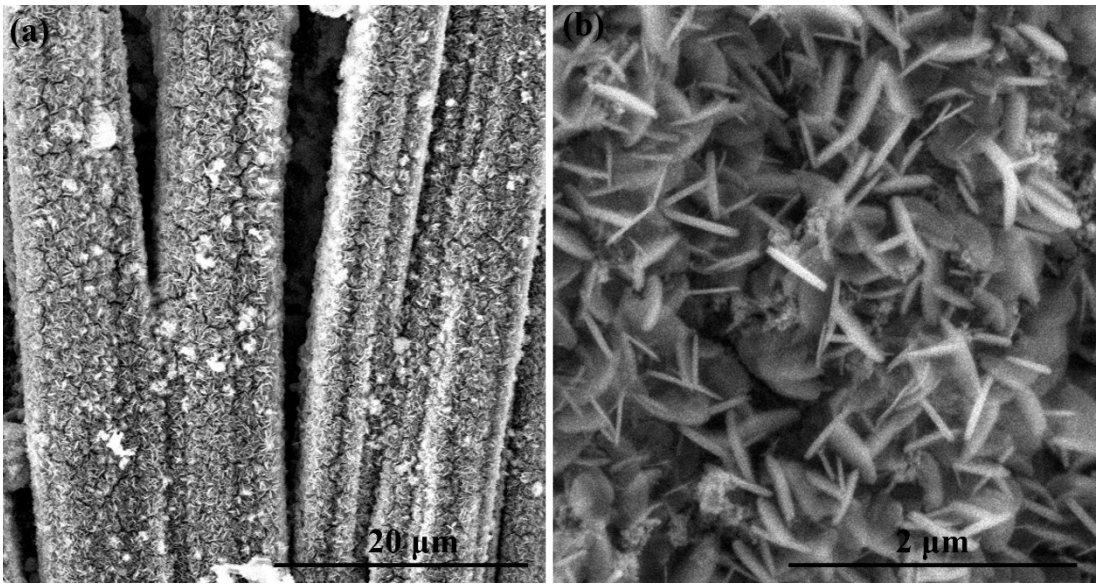

Figure S17. The (a) SEM image and (b) Amplificatory SEM image of r-CFO@CC after water splitting (r-CFO-WS) in 1.0 M KOH solution.

S13. XPS of r-CFO @ CC-WS

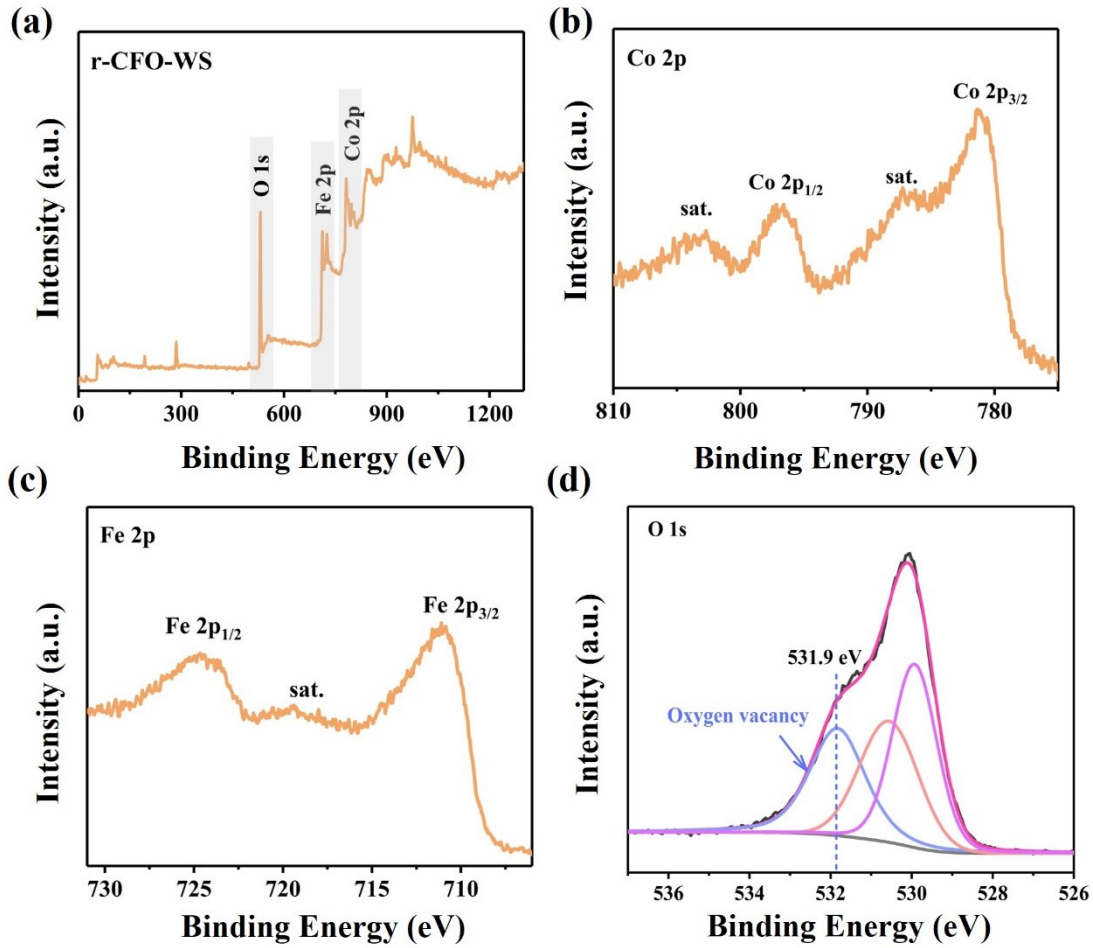

Figure S18. The XPS spectra of r-CFO-WS. (a) Survey spectrum, (b) Co 2p, (c) Fe 2p and (d) O 1s spectra of r-CFO after water splitting.

S14. XRD of r-CFO before and after reaction

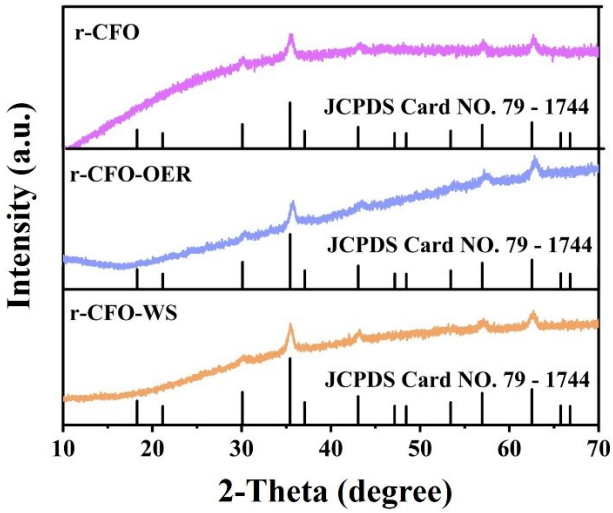

Figure S19. XRD patterns of r-CFO (the mauve line), r-CFO-OER (the wathet line) and r-CFO-WS (the orange line). The r-CFO-WS and r-CFO-OER was peeled off from the CC and GC after reaction, respectively.

S15. Electrocatalytic activity comparison of CFO, p-CFO and r-CFO

Table S1. Electrocatalytic activity comparison of CFO, p-CFO and r-CFO for OER.

	η^a /mV	Onset potential (V vs. RHE)	Tafel/ mV dec^{-1}	C_{dl} / mF cm^{-2}	R_{ct} [b]/ Ω	Number of acive sites / $\times 10^{-3}$ mol g^{-1}	TOF[c]/ s^{-1}
CFO	515	1.61	150	0.86	1790	1.06	0.007
p-CFO	410	1.58	82	1.55	519	3.03	0.013
r-CFO	280	1.46	43	3.28	36	6.86	0.207

a. The overpotential value when current density is 10 mA cm^{-2}.

b: Charge transfer resistance at 1.55 V.

c: The TOF value when current is 1.6 V vs. RHE.

Table S2. OER performance overview of typical reported spinel or anti spinel catalysts.

Spinel	Onset potential (V vs. RHE at 1 mA cm^{-2})	Over potential (V vs. RHE at 10 mA cm^{-2})	Tafel slope (mV dec^{-1})	Feature
r-CFO [This work]	**1.45**	**1.51**	**43**	**Nanosheets with oxygen vacancy and B-doped**

$CoFe_2O_4$ [6]	1.53	1.61	73	Nanoparticle grafted on carbon fiber papers
$CoFe_2O_4$ [7]	1.53	1.57	31	Grafted on rGO
$NiCo_2O_4$ [8]	1.46	1.52	53	Hierarchical hollow cuboids
$NiCo_2O_4$ [9]	1.52	1.69	90	Porous crystalline $NiCo_2O_4$ nanowire arrays
$CoFe_2O_4$ [10]	1.54	1.67	82.2	Nanofibers
$NiCo_2O_4$ [11]	1.55	1.60	30	Ultrathin nanosheets
$NiCo_2O_4$ [12]	1.56	1.60	60	$NiCo_2O_4/Ni_{0.33}Co_{0.67}S_2$ hybrids
Co_3O_4/ $NiCo_2O_4$ [13]	1.53	1.57	88	Double-shelled structure

Table S3. Electrocatalytic activity comparison of CFO, p-CFO and r-CFO for HER.

	η^a /mV	Onset potential (mV vs. RHE)	Tafel/ mV dec^{-1}	R_{ct} [b]/ Ω	Number of acive sites / $\times 10^{-3}$ mol g^{-1}	TOF[c]/ s^{-1}
CFO	351	-289	113	598	0.49	0.019
p-CFO	217	-122	98	357	1.12	0.044
r-CFO	121	-73	54	109	3.27	0.093

a. The overpotential value when current density is 10 mA cm^{-2}.

b: Charge transfer resistance.

c: The TOF value when current is -0.15 V vs. RHE.

Table S4. HER performance overview of reported catalysts.

	Over potential (mV vs. RHE at 10 mA cm^{-2})	Tafel slope (mV dec^{-1})	Feature
r-CFO This work	**121**	**54**	**Nanosheets with oxygen vacancy**
NiP_2/NiO NRs [14]	131	94	NiP_2/NiO nanorod arrays
Co_4Ni_1P NTs [15]	129	52	Nickel–cobalt bimetal phosphide nanotubes
N@MoPC [16]	139	86.6	N-doped porous Mo carbide and phosphide
HNDCM Co/CoP [17]	138	64	N-doped nanoporous carbon membranes with Co/CoP

			nanocrystals
CoP@NC [18]	129	58	Ultrathin N-doped carbon coated with CoP
NiCoP/rGO [19]	209	124.1	Ternary $Ni_{2-x}Co_xP$ with graphene
$Ni_{2-x}Co_xP$/N-C NFs [20]	130	30	Solid-solution-alloy engineering of $Ni_{2-x}Co_xP$

Table S5. Catalytic performance overview of typical reported bifunctional catalysts.

Bifunctional catalyst	Electrolyte	Potential (V at 10 mA cm^{-2})	Feature
r-CFO @ CC This work	**1 M KOH**	**1.53**	**Nanosheet arrays with oxygen vacancy grown on carbon cloth**
Co_1Mn_1CH/NF [21]	1 M KOH	1.68	Nanosheet arrays on nickel foam and Mn-doped
Ni-Co-P-HNBs [22]	1 M KOH	1.62	Oriented hollow nanobricks
Ni_3N-NiMoN [23]	1 M KOH	1.54	Heterostructures constructed by the controllable nitridation
Fe-Ni_3S_2/NF [24]	1 M KOH	1.54	Fe-doped Ni_3S_2 nanosheet array grown on 3D Ni foam
$Co_5Mo_{1.0}O$ NSs@NF//$Co_5Mo_{1.0}$PN Ss@NF [25]	1 M KOH	1.68	Nanosheet arrays on nickel foam and phosphorization
$NiCo_2S_4$ NA/CC [26]	1 M KOH	1.68	Nanowires array on carbon cloth
FeMnP/GNF [27]	1 M KOH	1.55	Deposition the FeMnP onto graphene-protected nickel foam
NiFe-NC [28]	1 M KOH	1.67	NiFe Prussian blue analog metal-organic framework

S16. Computational methods and detailed information

1. Computational methods

All DFT calculations were carried out using the Vienna *Ab initio* Simulation Package (VASP).[29, 30] The interaction between valence electron and ion core is described by the projector-augmented wave method (PAW).[31] The Perdew−Burke−Ernzerhof (PBE)[32] functional is applied to describe the electron exchange-correlation and the kinetic energy cutoff is 500 eV. The inverse spinel structure CFO with the experimental lattice parameter of 8.390 Å [33] was used for the unit cell consisting of 14 atoms. To account for the strong electron correlations in CFO, we employed the GGA + U with a $U - J$ value of 3.42 eV and 3.30 eV for the respective Fe and Co metal cations.[34] The CFO structure is ferromagnetic and the Néel configuration is chosen as the ground state, where the magnetic spins of tetrahedral and octahedral sites are opposite. In **Table S6**, the calculated total magnetic moment (M_{total}) was consistent with the experimental values reported.[35] For the calculations of density of states (DOS), a 9 × 9 × 9 k-mesh was used. Experimental study found that the CFO(113) surface with oxygen vacancies has a higher activity for the H_2O molecule. All geometries are optimized using Monkhorst−Pack kpoints with 3 × 3 × 1. The vacuum layer of 15 Å thickness was set to avoid the interaction between the periodic images. The atomic positions were optimized until the force on each atom was less 0.05 eV/Å and dipole corrections along the slab normal were considered.

We first optimized different CFO(113) structures with various terminations and the results showed that the CFO(113) structure in **Figure S21** is a thermodynamically stable surface. Different CFO(113) surfaces with one and two oxygen vacancies were constructed as shown in **Figure S21**. The active sites of the stable CFO(113) surface are considered to be octahedral Iron/cobalt centers and tetrahedral Iron center (Fe_{oct}, Co_{oct} and Fe_{tet}) as displayed in **Figure S22** and **Figure S23**. We calculated the adsorption energy according to the following equation:

$$E_{ads} = E_{adsorbate/slab} - (E_{adsorbate} + E_{slab})$$

Where $E_{adsorbate/slab}$, $E_{adsorbate}$, E_{slab} are the energy of the adsorbed system, the gas-phase molecule, and the CFO(113) surface, respectively. A negative value of E_{ads} indicates that the adsorption is exothermic. Similarly, dissociative adsorption energy for HO* and H* is defined as

$$\Delta E_{diss} = E_{dissociated\ adsorbate/slab} - (E_{adsorbate} + E_{slab})$$

From **Table S7**, it revealed that the oxygen vacancies have an important effect on $Fe1_{oct}$ atom.

The Gibbs free energy (G) of a species is calculated by

$$G = E + ZPE - TS$$

where E is the total energy of adsorbed species from DFT calculations, ZPE and S are the zero-point energy and entropy of a species respectively, and T = 298.15 K. Thermal corrections for gas molecules are from database.[36] Based on the computational hydrogen electrode model,[37] the Gibbs free-energy change (ΔG) is calculated as

$$\Delta G = \Delta E + \Delta \mathrm{ZPE} - T\Delta S$$

2. Magnetization of Co and Fe of inverse spinel CFO, CFO(113) and CFO(113) with oxygen vacancies

Here we compared the magnetic moments of the inverse spinel CFO bulk and surface atoms of CFO(113) and CFO(113) with oxygen vacancies.

Table S6. Calculated magnetic moments (μ_B) of Co, Fe and one formula unit of the inverse spinel CFO with unit cell consisting of 14 atoms.

System	Co_{oct}	Fe_{oct}	Fe_{tet}	M_{total}
Inverse spinel CFO	2.60	4.12	–4.00	3.00

Table S7. Calculated magnetic moments (μ_B) of surface Fe and Co atoms in the CFO(113) surface.

Surfaces	Co_{oct}	$Fe1_{oct}$ / $Fe2_{oct}$	Fe_{tet}
CFO	2.57	3.42/4.13	–3.95
CFO-1O_{vac}	2.63	4.03/4.10	–3.66
CFO-2O_{vac}	2.63	3.58/4.08	–3.62

3. Adsorption of H_2O molecules on the CFO

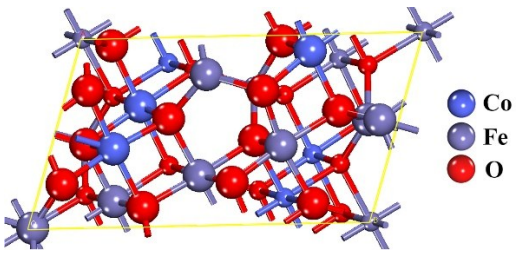

Figure S20. The model of CFO without oxygen vacancy.

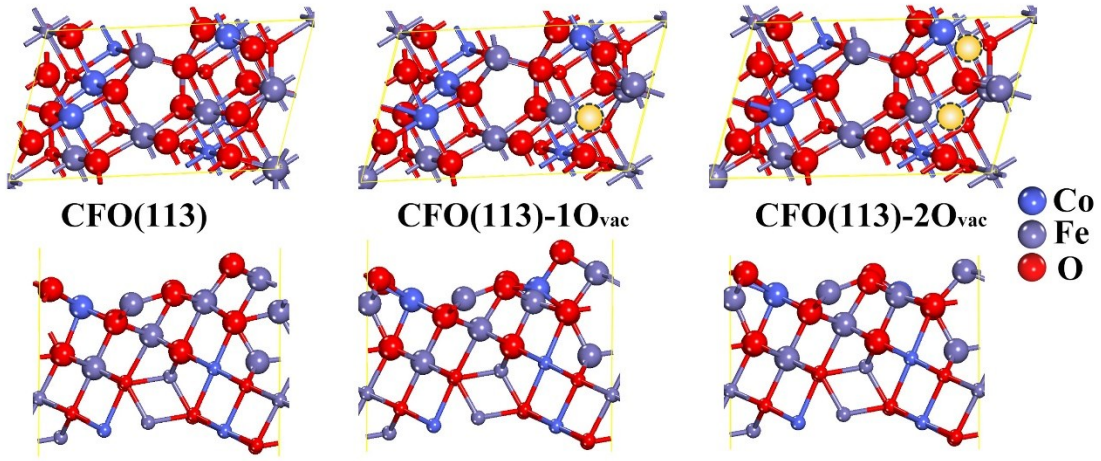

Figure S21. The optimized CFO, CFO-1O_{vac} and CFO-2O_{vac} (blue dotted circle) for a single unit cell with a periodic boundary (up: top view, down: side view).

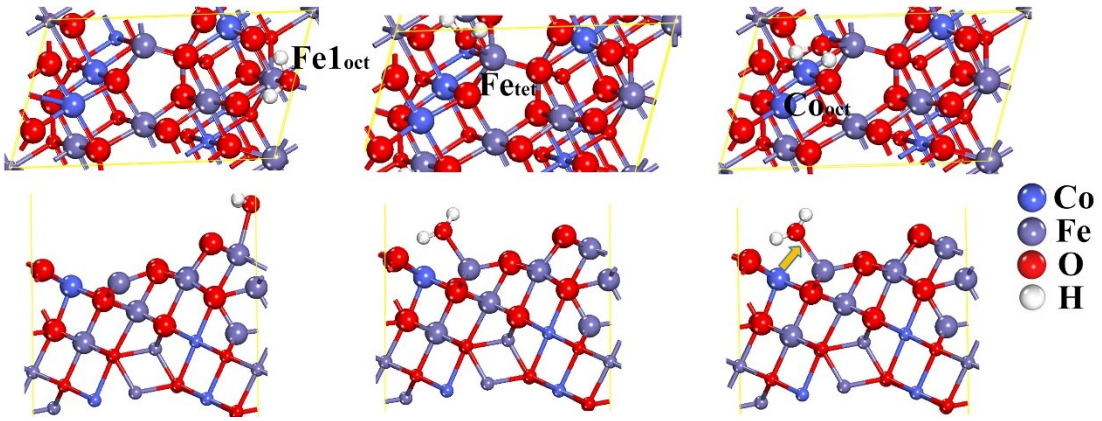

Figure S22. The optimized CFO-H_2O structures for H_2O molecules initially adsorbed onto Fe_{oct}, Fe_{tet} and Co_{oct} sites in the CFO (113) surface (up: top view, down: side view).

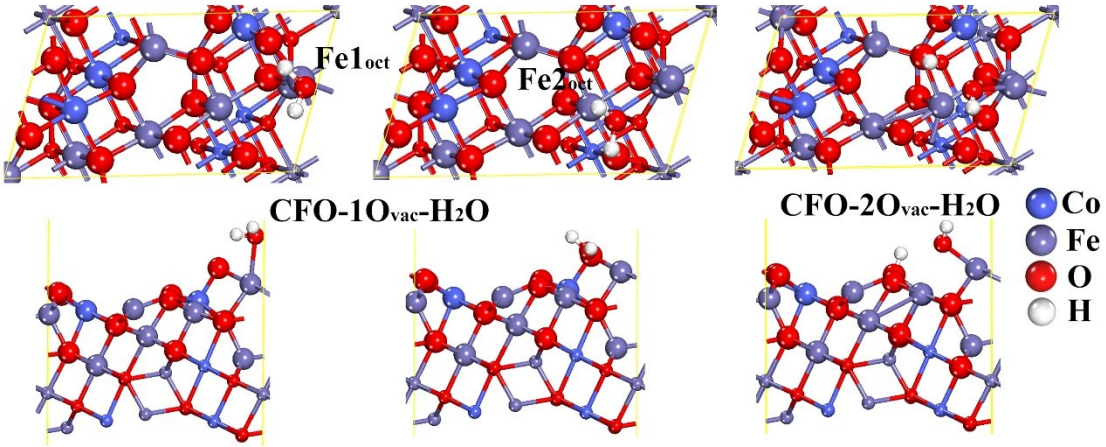

Figure S23. The optimized CFO(113)-O_{vac}-H_2O structures for H_2O molecules initially adsorbed onto **Fe_{oct} s**ites in the CFO-1O_{vac} and CFO-2O_{vac} surfaces (up: top view, down: side view).

Table S8. Adsorption energies (E_{ads}, eV) and dissociative adsorption energy (E_{diss}, eV) for H_2O molecule adsorbed onto CFO, CFO-1O_{vac} and CFO-2O_{vac} surfaces.

Surfaces	CFO			CFO- 1O_{vac}		Surfaces	CFO- 2O_{vac}
sites	Fe1$_{oct}$	Fe$_{tet}$	sites	Fe1$_{oct}$	Fe2$_{oct}$	sites	--
E_{ads}	–0.56	–1.27	E_{ads}	–0.70	–1.01	ΔE_{diss}	–1.59

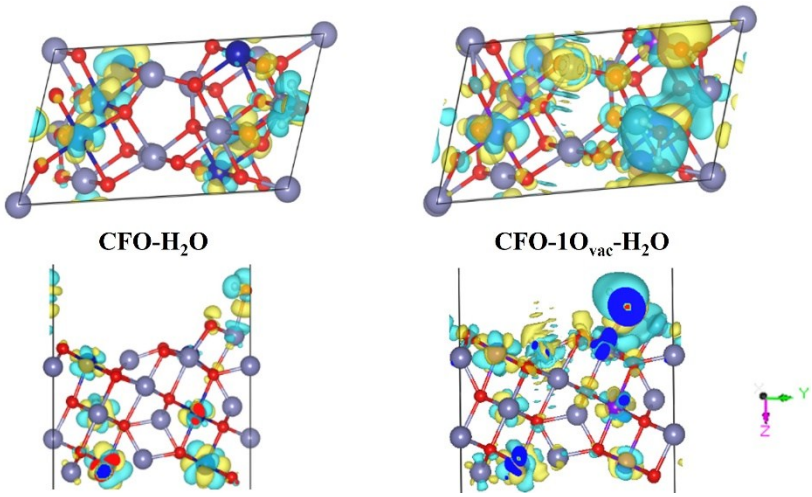

Figure S24. The difference charge density ($\Delta\rho = \rho_{surface–H2O} - \rho_{surface} - \rho_{H2O}$) for the CFO-$H_2O$ and CoFO-1O_{vac}-H_2O systems with H_2O chemisorption on Fe1$_{oct}$ and Fe2$_{oct}$ sites, respectively. (up: top view, down: side view).

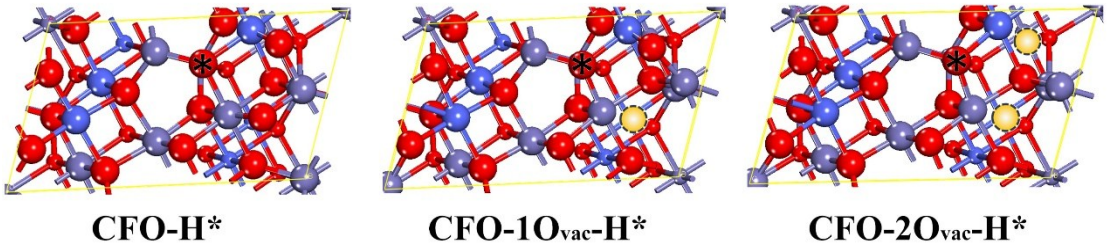

Figure S25. Top view of H adsorption sites (*) on CFO, CFO-1O_{vac} and CFO-2O_{vac} surfaces.

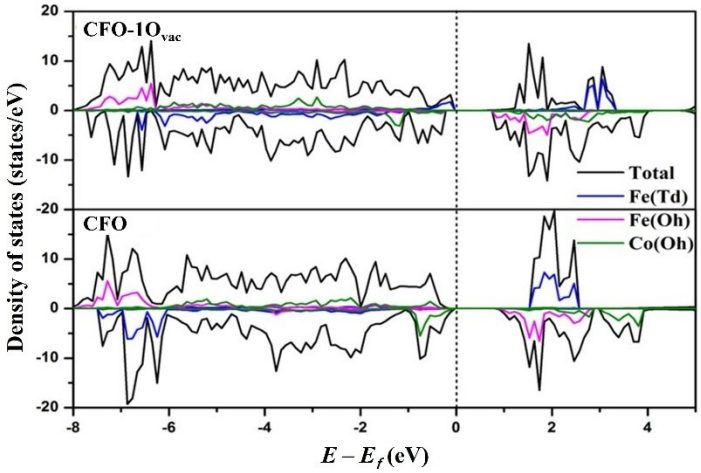

Figure S26. The atom-projected density of states and total DOS of CFO-1O_{vac} with one oxygen vacancy and the inverse spinel structure CFO. The positive and negative parts denote the majority spin and the minority spin, respectively.

S17. Solid ultraviolet spectrum of CFO, p-CFO as well as r-CFO

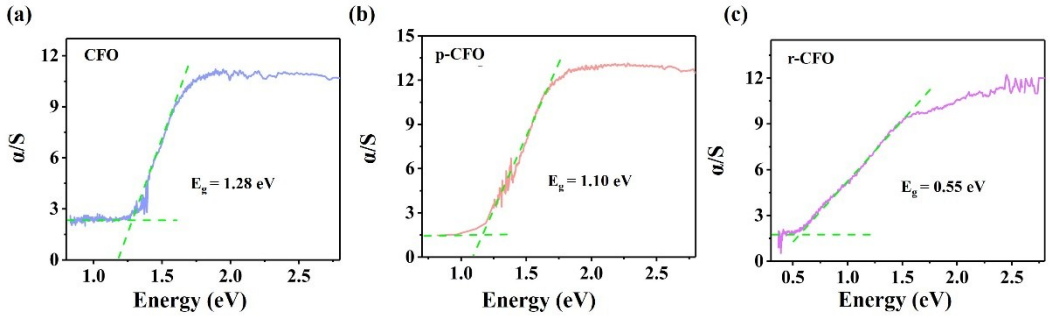

Figure S27. Solid ultraviolet spectrum of (a) CFO, (b) p-CFO as well as (c) r-CFO.

References

[1] J. F. Xie, S. Li, X. D, Zhang, J. J. Zhang, R. X. Wang, H. Zhang, B. C. Pan and Y. Xie, Chem. Sci. **2014**, 5, 4615–4620.

[2] T. V.Tam, S. G. Kang, K. F. Babu, E. Oh, S. G. Lee and W. M. Choi, J. Mater. Chem. A, **2017**, 5, 10537–10543.

[3] J. Y. Li, M. Yan, X. M. Zhou, Z. Q. Huang, Z. M. Xia, C. R. Chang, Y. Y. Ma, and Y. Q. Qu, Adv. Funct. Mater. **2016**, 26, 6785-6796.

[4] M. Gao, W. Sheng, Z. Zhuang, Q. Fang, S. Gu, J. Jiang and Y. Yan, *J. Am. Chem. Soc.* **2014**, 136, 7077-7084.

[5] L. Wu, Q. Li, C. H. Wu, H. Zhu, A. Mendoza-Garcia, B. Shen, J. Guo and S. Sun, *J. Am. Chem. Soc.* **2015**, 137, 7071-7074.

[6] A. Kargar, S. Yavuz, T. K. Kim, C. H. Liu, C. Kuru, C. S. Rustomji, S. Jin and P. R. Bandaru, *ACS Appl. Mater. Interfaces* **2015**, 7, 17851-17856.

[7] J. Geng, L. Kuai, E. Kan, Q. Wang and B. Geng, *ChemSusChem*. **2015**, 8, 659-664.

[8] X. Gao, H. Zhang, Q. Li, X. Yu, Z. Hong, X. Zhang, C. Liang and Z. Lin, *Angew. Chem. Int. Ed.* **2016**, 55, 6290-6294.

[9] X. Yu, Z. Sun, Z. Yan, B. Xiang, X. Liu and P. Du, *J. Mater. Chem. A* **2014**, 2, 20823-20831.

[10] M. Li, Y. Xiong, X. Liu, X. Bo, Y. Zhang, C. Han and L. Guo, *Nanoscale* **2015**, 7, 8920-8930.

[11] J. Bao, X. Zhang, B. Fan, J. Zhang, M. Zhou, W. Yang, X. Hu, H. Wang, B. Pan and Y. Xie, *Angew. Chem. Int. Ed.* **2015**, 54, 7399-7404.

[12] Z. Peng, D. Jia, A. M. Al-Enizi, A. A. Elzatahry and G. Zheng, *Adv, Energy Mater,* **2015**, 5, 1402031.

[13] H. Hu, B. Y. Guan, B. Y. Xia, X. W. Lou, *J. Am. Chem. Soc.* **2015**, 137, 5590−5595.

[14] M. Y. Wu, P. F. Da, T. Zhang, J. Mao, H. Liu and T. Ling, *ACS Appl. Mater. Interfaces*, **2018**, 10, 17896-17902.

[15] L. Yan, L. Cao, P. Dai, X. Gu, D. Liu, L. Li, Y. Wang and X. Zhao, *Adv. Funct. Mater.*, **2017**, 27, 1703455.

[16] Y. Huang, J. Ge, J. Hu, J. Zhang, J. Hao and Y. Wei, *Adv. Energy Mater.*, **2018**, 8, 1701601.

[17] H. Wang, S. Min, Q. Wang, D. Li, G. Casillas, C. Ma, Y. Li, Z. Liu, L. J. Li, J. Yuan, M. Antonietti and T. Wu, *ACS Nano.*, **2017**, 11, 4358-4364.

[18] F. Yang, Y. Chen, G. Cheng, S. Chen and W. Luo, *ACS Catal.*, **2017**, 7, 3824-3831.

[19] J. Li, M. Yan, X. Zhou, Z.-Q. Huang, Z. Xia, C.-R. Chang, Y. Ma and Y. Qu, *Adv. Funct. Mater.*, **2016**, 26, 6785-6796.

[20] Q. Mo, W. Zhang, L. He, X. Yu and Q. Gao, *Appl. Catal. B: Environ.*, 2019, **244**, 620-627.

[21] T. Tang, W. J. Jiang, S. Niu, N. Liu, H. Luo, Y. Y. Chen, S. F. Jin, F. Gao, L. J. Wan, J. S. Hu, *J. Am. Chem. Soc.* **2017**, 139, 8320−8328.

[22] E. Hu, Y. Feng, J. Nai, D. Zhao, Y. Hu and X. W. Lou, *Energ. Environ. Sci.* **2018**, 11, 872-880.

[23] A. Wu, Y. Xie, H. Ma, C. G. Tian, Y. Gu, H. J. Yan, X. M. Zahng, G. Y. Yang, H. G. Fu, *Nano Energy* **2018**, 44, 353–363.

[24] G. Zhang, Y.-S. Feng, W.-T. Lu, D. He, C.-Y. Wang, Y.-K. Li, X.-Y. Wang and F.-F. Cao, *ACS Catal.* **2018**, 8, 5431-5441.

[25] Y. Zhang, Q. Shao, S. Long and X. Huang, *Nano Energy* **2018**, 45, 448-455.
[26] D. Liu, Q. Lu, Y. Luo, X. Sun and A. M. Asiri, *Nanoscale* **2015**, 7, 15122-15126.
[27] Z. Zhao, D. E. Schipper, A. P. Leitner, H. Thirumalai, J.-H. Chen, L. Xie, F. Qin, M. K. Alam, L. C. Grabow, S. Chen, D. Wang, Z. Ren, Z. Wang, K. H. Whitmire and J. Bao, *Nano Energy* **2017**, 39, 444-453.
[28] A. Kumar and S. Bhattacharyya, *ACS Appl. Mater. Interfaces* **2017**, 9, 41906-41915.
[29] G. Kresse, J. Furthmüller, *Phys. Rev. B: Condens. Matter. Mater. Phys.* **1996**, 54, 11169−11186.
[30] G. Kresse, J. Furthmüller, *Comput. Mater. Sci.* **1996**, 6, 15−50.
[31] P. E. Blöchl, *Phys. Rev. B: Condens Matter. Mater. Phys.* **1994**, 50, 17953.
[32] J. P. Perdew, K. Burke, M. Ernzerhof, *Phys. Rev. Lett.* **1996**, 77, 3865.
[33] R. Wyckoff, *Wiley-interscience*,**1964**.
[34] I. V. Solovyev, P. H. Dederichs, V. I. Anisimov, *Phys. Rev. B*, **1994**, 50, 16861.
[35] Y. H. Hou, Y. J. Zhao, Z. W. Liu, *J Phys D: Appl. Phys.* **2010**, 43, 445003.
[36] D.R. Lide, *CRC Press: Boca Raton FL*, **2004**.
[37] E. Skúlason, T. Bligaard, S. Gudmundsdóttir, F. Studt, J. Rossmeisl, F. Abild-Pedersen, T. Vegge, H. Jónsson, J. K. Nørskov, *Phys. Chem. Chem. Phys.,* **2012**, 14, 1235-1245.